Earthquakes on Dipping Faults: The Effects of Broken Symmetry

David D. Oglesby, *et al.*

Science **280**, 1055 (1998);
DOI: 10.1126/science.280.5366.1055

Science (print ISSN 0036-8075; online ISSN 1095-9203) is published weekly, except the last week in December, by the American Association for the Advancement of Science, 1200 New York Avenue NW, Washington, DC 20005.

scale of less than 60 days (*22*).

Our data for EP96B1 and EP96B2 thus show that this event plume changed very slowly after it formed. In many plumes from the southern JdFR, light attenuation anomaly, assumed to be produced mainly by suspended particulate Fe, could be detected more than 20 km away from the source, indicating a long residence time for particulate Fe (*35*). Using radon as a clock, Kadko *et al.* (*32*) studied the removal rates of various hydrothermal constituents from the Endeavour Ridge effluent plume. They observed no measurable change in Mn concentrations with time and were only able to place a lower limit of $\tau \geq 20$ days for the residence time of total Mn (*36*). Our measurements indicate that light-scattering anomaly, particulate Fe, and dissolved Mn decreased by no more than 15% during the 60-day RAFOS experiment, indicating a residence time $\tau \geq 1$ year for these three hydrothermal tracers (*33*). For Fe, this estimate is similar to what has been found for steady-state plumes (*37*).

Future experiments might track an event plume for a year or more with several RAFOS floats programmed to surface at various stages in the plume evolution. Alternatively, floats equipped with acoustic transponders would allow surface ships to range on the floats, thereby eliminating the necessity of having the floats surface to locate the plume.

REFERENCES AND NOTES

1. E. T. Baker, G. J. Massoth, R. A. Feely, *Nature* **329**, 149 (1987).
2. J. W. Lavelle, *Geophys. Res. Lett.* **22**, 159 (1995).
3. R. W. Embley, W. W. Chadwick Jr., M. R. Perfit, E. T. Baker, *Geology* **19**, 771 (1991).
4. R. W. Embley, W. W. Chadwick Jr., I. R. Jonasson, D. A. Butterfield, E. T. Baker, *Geophys. Res. Lett.* **22**, 143 (1995).
5. R. W. Embley and W. W. Chadwick Jr., *J. Geophys. Res.* **99**, 4741 (1994).
6. E. D'Asaro, S. Walker, E. T. Baker, *ibid.*, p. 20361.
7. L. S. Mullineaux and S. C. France, in *Seafloor Hydrothermal Systems: Physical, Chemical, Biological, and Geological Interactions*, S. E. Humphris, R. A. Zierenberg, L. S. Mullineaux, R. E. Thomson, Eds. [American Geophysical Union (AGU), Washington, DC, 1995], pp. 408–424; L. S. Mullineaux, P. H. Wiebe, E. T. Baker, *Oceanus* **34**, 64 (1991).
8. E. T. Baker *et al.*, *Geophys. Res. Lett.* **22**, 147 (1995).
9. E. T. Baker, in preparation.
10. K. G. Speer, *Geophys. Res. Lett.* **16**, 461 (1989).
11. K. R. Helfrich and K. G. Speer, in *Seafloor Hydrothermal Systems: Physical, Chemical, Biological, and Geological Interactions*, S. E. Humphris, R. A. Zierenberg, L. S. Mullineaux, R. E. Thomson, Eds. (AGU, Washington, DC, 1995), pp. 347–356.
12. K. R. Helfrich and T. M. Battisti, *J. Geophys. Res.* **96**, 12511 (1991).
13. J. C. McWilliams, *Rev. Geophys.* **23**, 165 (1985).
14. L. Armi *et al.*, *J. Phys. Oceanogr.* **19**, 354 (1989).
15. RAFOS is not an acronym but is SOFAR spelled backward. SOFAR (Sound Fixing and Ranging) floats emit sounds that are detected by fixed hydrophones, which is the opposite of the method of the RAFOS floats.
16. C. G. Fox and R. P. Dziak, in preparation.
17. Three different response cruises documented the effects of the 1996 Gorda Ridge event on the ocean water column and sea floor. These expeditions are now referred to as GREAT 1, 2, and 3, after the Gorda Ridge Event Assessment Team.
18. J. E. Lupton, unpublished data.
19. D. S. Kelley, M. D. Lilley, J. E. Lupton, E. J. Olson, *Deep-Sea Res.*, in press.
20. R. Feely *et al.*, *ibid.*, in press.
21. G. J. Massoth *et al.*, *ibid.*, in press.
22. J. P. Cowen *et al.*, *ibid.*, in press.
23. W. W. Chadwick Jr. and R. W. Embley, in preparation.
24. The apparent excess heat is reported in the form of temperature anomaly $\Delta\theta$, which is the deviation of the potential temperature θ from the ambient θ versus potential density (σ_θ) relation, which is linear for the deep waters of the northeast Pacific. Thus, $\Delta\theta = \theta - k\sigma_\theta - b$, where k and b are, respectively, the empirically determined slope and intercept of the θ versus σ_θ line.
25. J. E. Lupton, E. Baker, G. Massoth, *Nature* **337**, 161 (1985); J. E. Lupton *et al.*, *Geophys. Res. Lett.* **22**, 155 (1995).
26. H. T. Rossby, D. Dorson, J. Fontaine, *J. Atmos. Ocean. Tech.* **3**, 672 (1986).
27. S. Pond and G. L. Pickard, *Introductory Dynamic Oceanography* (Pergamon, Oxford, UK, 1978), p. 120.
28. Here $\Omega = 7.29 \times 10^{-5}$ rad s^{-1}, the angular velocity of Earth's rotation, and ϕ = latitude. The minus sign for the relative vorticity of the event plumes indicates an anticyclonic sense of rotation.
29. For event plume EP96B2, we calculate the internal Rossby radius to be ~30 km, which is considerably larger than the radius of the plume itself, which was ~5 km. Thus, the event plume was a submesoscale feature.
30. G. J. Massoth *et al.*, *J. Geophys. Res.* **99**, 4905 (1994).
31. J. W. Lavelle, J. P. Cowen, G. J. Massoth, *ibid.* **97**, 7413 (1992); C. S. Chin *et al.*, *ibid.* **99**, 4969 (1994).
32. D. C. Kadko, N. D. Rosenberg, J. E. Lupton, R. C. Collier, M. D. Lilley, *Earth Planet. Sci. Lett.* **99**, 315 (1990).
33. We quantified changes in light scattering, ^{3}He concentration, particulate Fe, and dissolved Mn between EP96B1 and EP96B2 by means of separate linear regression fits to each of these properties versus $\Delta\theta$ (Fig. 7). In each case, the linear regression fits gave slopes for EP96B1 and EP96B2 that agreed within one standard deviation. The slopes for EP96B1 and EP96B2 differed at most by 15%, a difference we attribute to measurement errors. This 15% difference is the basis for lower limit calculated for the residence time of these properties.
34. J. P. Cowen and Y. H. Li, *J. Mar. Res.* **49**, 517 (1991); J. F. Gendron, J. P. Cowen, R. A. Feely, E. T. Baker, *Deep-Sea Res. I* **40**, 1559 (1993).
35. E. T. Baker and G. J. Massoth, *Earth Planet Sci. Lett.* **85**, 59 (1987).
36. The residence time τ is defined as the time for the concentration to be reduced to 1/e or 0.368 of its original value, assuming that the concentration of property X decays exponentially as $X(t) = X_0 e^{-t/\tau}$.
37. R. A. Feely *et al.*, *Geochim. Cosmochim. Acta* **60**, 2297 (1996).

38. We thank G. Lebon, J. Gendron, S. Maenner, J. Resing, E. Olson, X. Wen, D. Tennant, and the officers and crews of the *NOAA Ship MacArthur*, the *R/V Wecoma*, and the *NOAA Ship Discoverer* for assistance with the sample collections at sea; S. Walker for assistance in the collection and analysis of the hydrographic data; and L. Evans, G. Lebon, J. Gendron, S. Maenner, and X. Wen for the analysis of water samples. J. Waddell provided valuable editorial assistance. The paper profited from discussions with C. Collins and G. Cannon and from reviews by two anonymous reviewers. This research was funded by the NOAA VENTS Program, by NSF grant OCE93-20240 to the Monterey Naval Postgraduate School, and by NSF grant OCE96-34637 to the University of Hawaii. This is Pacific Marine Environmental Laboratory contribution number 1932.

21 January 1998; accepted 17 March 1998

Earthquakes on Dipping Faults: The Effects of Broken Symmetry

David D. Oglesby, Ralph J. Archuleta,* Stefan B. Nielsen

Dynamic simulations of earthquakes on dipping faults show asymmetric near-source ground motion caused by the asymmetric geometry of such faults. The ground motion from a thrust or reverse fault is larger than that of a normal fault by a factor of 2 or more, given identical initial stress magnitudes. The motion of the hanging wall is larger than that of the footwall in both thrust (reverse) and normal earthquakes. The asymmetry between normal and thrust (reverse) faults results from time-dependent normal stress caused by the interaction of the earthquake-generated stress field with Earth's free surface. The asymmetry between hanging wall and footwall results from the asymmetric mass and geometry on the two sides of the fault.

Historically, much earthquake research in the United States has focused on large vertical strike-slip faults such as the San Andreas Fault in California. However, for compressive tectonic regimes such as the Los Angeles area, Japan, and Central and South America, and in extensional regimes such as the Mediterranean and the Great Basin of Nevada, Utah, and Idaho, seismic hazard lies in nonvertical (dipping) faults (*1*). One difference between a vertical and a nonvertical fault is the breakdown of symmetry with respect to the free surface in the nonvertical case (Fig. 1). Because of this geometrical asymmetry, the earthquake-generated stress field must change to match

D. D. Oglesby and R. J. Archuleta, Institute for Crustal Studies and Department of Geological Sciences, University of California at Santa Barbara, Santa Barbara, CA 93106, USA.
S. B. Nielsen, Institute for Crustal Studies and Materials Research Laboratory, University of California at Santa Barbara, Santa Barbara, CA 93106, USA.

*To whom correspondence should be addressed.

the stress boundary at the free surface. This interaction causes variations in the normal stress on the fault. The variations in the normal stress affect the friction and hence the dynamic rupture of the earthquake. The net result is that the time-dependent normal stress produces asymmetric ground motion in the proximity of the fault.

Analyses of ground motion caused by recent thrust (reverse) and normal earthquakes (*2*) have tended to reinforce this view. The 1994 Northridge earthquake produced systematically higher ground motion on the hanging wall than on the footwall (*3*), and the 1971 San Fernando earthquake caused systematically greater damage and soil disturbance on the hanging wall (*4*). Nason (*5*) attributed these effects in the 1971 San Fernando earthquake to waves trapped in the hanging wall. Models of this earthquake (*6*) required slip of up to 8 m at shallow depth to explain the observed strong-motion recordings. Such large slip has also been seen in Brune's recent foam-rubber analog models of thrust faults (*7*). There is also evidence that thrust faults produce larger ground motion than normal faults (*8*). Here we provide a dynamic physical explanation of the observations (*3*–*8*) to gain insight into the possible ground motion from nonvertical dip-slip faults.

Using a two-dimensional finite element method (*9*), we simulated the dynamics of thrust and normal faults. The simulations include all elastic waves, and unlike most dynamic earthquake simulations (*10*), the models also include the time-dependent normal stress on the fault that results from the asymmetric geometry. We simulated thrust and normal faults with dip angles of 30°, 45°, and 60° (Fig. 1). For any given dip angle, the initial stresses, friction laws, and nucleation are the same for the thrust and normal faulting cases, with the exception of the sign of the shear stress (*11*). The friction law is a time-dependent stress drop, in which the fault is held together by static friction until the fault reaches its yield stress, at which time the frictional stress drops smoothly to the sliding frictional level (*12*). The fault heals when the slip rate goes to zero. Once the fault is healed, it is constrained not to slip again regardless of the stress level.

Time-dependent normal stress and its explicit inclusion in our friction law causes the difference in fault and ground motion between thrust and normal faulting in the dynamic simulations. This effect can be illustrated by considering the geometry, stress definitions, and coordinate system of Fig. 1 and a point on the fault at the surface of Earth where the free-surface stress conditions apply:

$$\sigma_x^f = 2\sigma_x$$
$$\sigma_y^f = 0$$
$$\sigma_{xy}^f = 0 \qquad (1)$$

The superscript f refers to the values at the free surface, and σ_x refers to stress in the x direction in a whole space. In the absence of a free surface, rupture of the fault at depth would cause a change in shear stress $\Delta\tau$ at our point on the fault. The standard Amonton criterion for fracture is $|\tau| \geq -\mu\sigma_n$, where τ is the shear stress on the fault, σ_n is the normal stress across the fault, and μ is the static coefficient of friction. Thus, if we write a failure criterion $C = |\tau| + \mu\sigma_n$, then the fault will fail when $C > 0$. In a whole space the rupture at depth would bring our point closer to failure by an amount $\Delta C = \Delta\tau$. However, the free surface causes the stress field due to the fault rupture

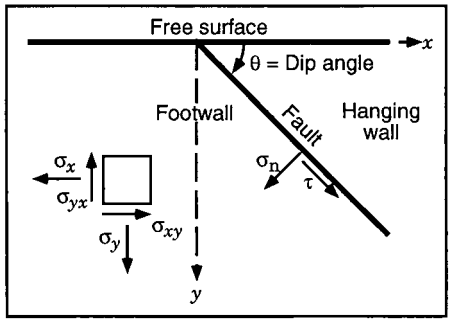

Fig. 1. Schematic diagram of the geometry and coordinate system of the fault models, as described (*2*). For a nonvertical (dipping) fault such as presented here, the symmetry between the two sides of the fault and the free surface is broken.

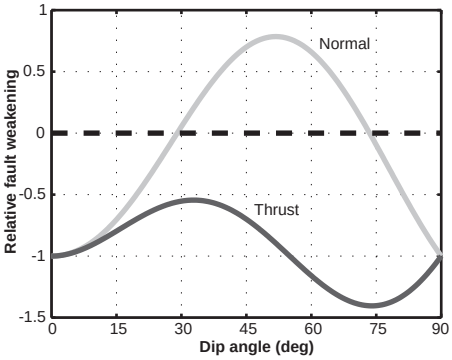

Fig. 2. The relative fault weakening $(C^f - C)/\tau$ ahead of the crack tip at the free surface, due to fault slip at depth. $\mu = 0.7$ [an average value for the static friction coefficient from Byerlee's Law (*24*)]. A relative fault weakening of zero corresponds to the case where there is no free surface, so symmetry is not broken. With respect to the no-free-surface case, weakening >0 represents aiding the rupture, and weakening <0 represents hindering the rupture. However, any relative fault weakening > -1 corresponds to bringing the fault closer to rupture in an absolute sense.

at depth to rotate to match the stress conditions (Eq. 1) at our point. The change in rupture criterion $C^f - C$ due to the presence of the free surface (*13*) will depend on whether τ is negative (as in a normal fault) or positive (as in a thrust fault). For a normal fault (dropping the delta notation and letting all stresses below correspond to stress perturbations due to earthquake rupture):

$$C^f - C = -|\tau|\cos^2(2\theta) + 4\mu|\tau|\sin^3(\theta)\cos(\theta) \qquad (2)$$

whereas for a thrust fault

$$C^f - C = -|\tau|\cos^2(2\theta) - 4\mu|\tau|\sin^3(\theta)\cos(\theta) \qquad (3)$$

When $C^f - C > 0$, the fault is brought closer to failure near the free surface than it would have been in the absence of the free surface; the opposite holds for $C^f - C < 0$ (Fig. 2).

One consequence of the free-surface boundary condition on stress is that for normal faults with dip angles between about 30° and 75°, slip farther down-dip on the fault brings the fault near the free surface closer to failure than it would have been in a whole space. This effect is predominantly due to the decrease in σ_n with a resultant decrease in the yield frictional stress. In some circumstances this effect can lead to the rupture front jumping ahead (a secondary nucleation) near the free surface of a normal fault (*13*).

The opposite is true for a thrust fault: It is brought further from failure than it would have been in a whole space, primarily due to an increase in the normal stress with a

Table 1. Fault and material parameters. V_p, *P*-wave velocity; V_s, *S*-wave velocity.

Fault width (down-dip)	28.28 km
Fault dip	30°, 45°, 60°
Shear prestress	2.8 MPa
Normal prestress	6.0 MPa
Static frictional coefficient	0.7
Sliding frictional coefficient	0.3
Density	3000 kg/m^3
Shear modulus	30000 MPa
Poisson's ratio	0.25
V_p	5.48 km/s
V_s	3.16 km/s

Table 2. Computational parameters.

Element width on fault	141.4 m
Time increment	1.5×10^{-3} s
Maximum frequency	~2 Hz
Critical slip time	0.2 s
Total time	20 s
Number of elements	~96,000
Run time (UltraSparc 30)	~3 to 4 hours

consequent increase in the static frictional stress holding the fault locked. However, over most of the range in dip angle, the fault is still brought toward failure; it is merely not brought as close to failure as it would have been without the free surface.

Ahead of the crack tip, as a result of the shear-stress increase, the normal-stress change is tensional for a normal fault and compressional for a thrust fault. Behind the crack tip, in the slipping region of the fault, the stress changes are of opposite sign because of the drop from static to sliding friction on the fault. Therefore, the effect of the free surface on σ_n also changes sign: In the slipping region near the free surface, the normal stress on a normal fault is increased, whereas it is decreased for a thrust fault.

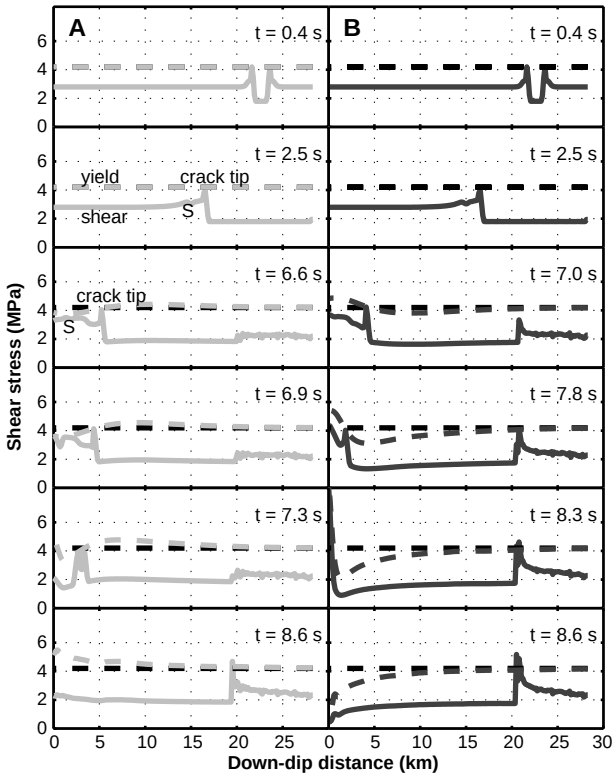

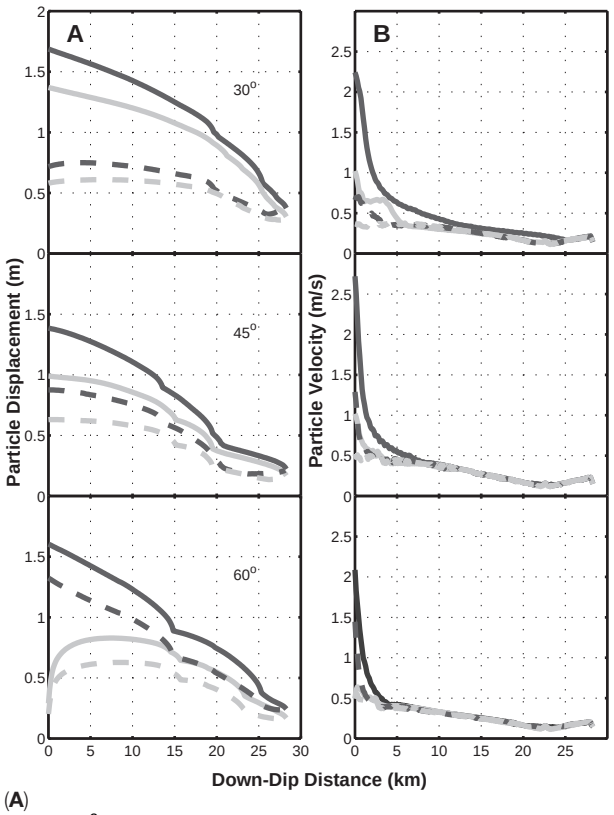

Fig. 3 (top left). Snapshots of stresses calculated for a 45° dipping normal fault (**A**) and thrust fault (**B**). Solid curves are the shear (frictional) stress on the fault, and dashed curves are the yield stress on the fault. The horizontal dashed line marks what the yield stress would be without the effect of the free surface. Zero on the horizontal axis corresponds to the free surface, and 28.3 km corresponds to the deepest part of the fault. The shear stress on the lower part of the faults exceeds the yield stress for times late in the simulations. This effect is due to the requirement that the fault not slip again after it has healed (stopped slipping). **Fig. 4 (top right).** Peak particle displacements (**A**) and velocities (**B**) on the fault planes of 30°, 45°, and 60° dipping faults. Zero on the horizontal axis corresponds to the free surface, and 28.3 corresponds to the deepest part of the fault. Dark curves denote thrust faults, and light curves denote normal faults. Solid curves denote hanging walls, and dashed curves denote footwalls. In all cases the initial stress conditions are identical, except for the sign of the shear stress. **Fig. 5 (bottom right).** Peak particle displacements (**A**) and velocities (**B**) on the surface near 30°, 45°, and 60° dipping faults. Going from negative to positive distance corresponds to going along the surface from the footwall, over the fault trace, to the hanging wall. Dark curves denote thrust faults, and light curves denote normal faults.

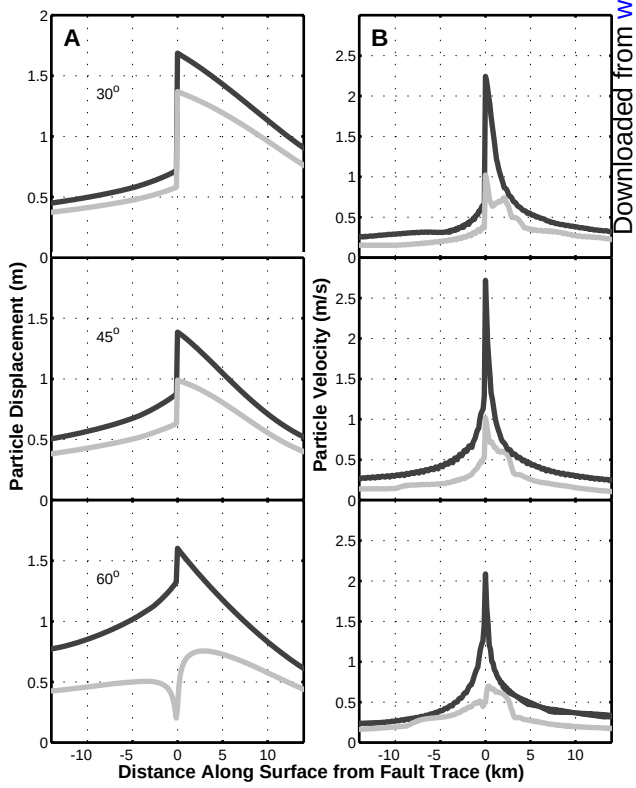

After starting to slip, a normal fault will have a stronger frictional force holding it back and have decreased particle motion. Conversely, a thrust fault will have lower friction, a greater stress drop, and increased particle motion.

This analytical development is valid only for the near-surface (within 1 wavelength) region where the free-surface stress conditions apply. It does not explain quantitatively the effect of the free surface on deeply buried (>1 wavelength) parts of the fault, especially after they have started to slip. It also does not take into account the effect of trapped waves in the hanging wall. However, as shown below, the effect of the free surface is manifested even at depth because of reflected waves from the free surface.

Our analytical model provides a way to interpret the results of the numerical simulation of dipping normal and thrust faults (Fig. 3 and Tables 1 and 2). Both faults nucleate at the same point near the deepest part of the fault and rupture up-dip toward the free surface. Initially the stresses are identical because the rupture is far from the free surface. At $t = 2.5$ s, we see a propagating crack (*14*): As the crack is approached from the left (traveling down-dip on the fault), a gradual increase in shear stress τ is apparent and a small peak corresponding to the *S* wave. A short distance down-dip, τ rises to the yield-stress level at the tip of the crack. Behind the crack tip, in the slipping region of the fault, τ drops to the sliding frictional-stress level. As the crack approaches the free surface, the normal and yield stresses for the two faults diverge. The normal and yield stresses on the normal fault decrease ahead of the crack tip, and increase behind it. At $t = 6.9$ s, the yield stress for the normal fault dips to the level of the *S*-wave stress ahead of the crack tip, causing nucleation of a secondary rupture front that propagates bilaterally up-dip toward the free surface and down-dip to meet the primary rupture front. After the rupture has covered the whole fault, τ and σ_n are higher near the free surface than at depth, inhibiting slip near the free surface.

The thrust fault shows the opposite effect on σ_n. Ahead of the crack tip at $t = 7.0$ s, σ_n and the yield stress are increased; behind the crack tip σ_n and the sliding frictional stress τ are decreased. This effect becomes much more pronounced as the rupture front approaches the free surface; an amplified stress drop occurs between 8.3 and 8.6 s. This large stress drop amplifies the particle motion on the fault and the resultant seismic radiation. Once the whole fault has started to slip, τ and σ_n decrease near the free surface, enhancing slip. This result is consistent with quasi-static simulations of dip-slip faulting (*15*). The large stress drop at the free surface may correspond to a breakout phase (*16*).

The peak particle displacements and velocities for faults with 30°, 45°, and 60° dips as a function of position on the fault (Fig. 4) show that the thrust faults have larger particle motions than normal faults, and the hanging walls have larger particle motion than the footwalls. The additional motion of the hanging wall is due to the fault geometry asymmetry: The hanging wall has less mass in the vicinity of the free surface than the footwall, so the same force will accelerate the hanging wall to a greater extent. Moreover, while the fault is slipping, it is essentially opaque to shear energy, trapping radiated waves in the hanging wall and further amplifying its motion. This effect of increased hanging wall motion was documented in lattice model simulations (*17*), as well as the quasi-static analysis of antiplane dipping faults (*18*). The contrast between hanging wall and footwall motion decreases as the dip increases toward 90°. The finite element results agree with those obtained from the finite difference method (*13*) for a 45° dipping fault.

The effect of the free surface decreases with depth, but the effect is different for the peak velocities and peak displacements. For the peak velocities at depth, the behavior of the hanging walls and footwalls of all the faults is the same. However, the displacements show asymmetry to even the bottom of the fault. The asymmetric displacement is caused by the thrust-fault breakout phase reflecting back down the fault, transmitting the effect of the free surface to every point on the fault. In the case of the 30° dipping thrust fault, this breakout phase is also responsible for the larger peak velocity in the hanging wall of the thrust fault at depth (Fig. 4). The decreased particle motion near the free surface for the 60° dipping normal fault is an artifact (*19*) of the greatly increased postrupture normal stress, which causes premature healing at the free surface.

In all cases the thrust fault produces higher ground motion than the normal fault on the free suface above the fault (Fig. 5), and there is a large discontinuity in particle displacement and velocity as one crosses from the footwall to the hanging wall. The consistently higher ground motion for the thrust faults is caused by the larger displacement on the fault in the thrust case and the resultant higher seismic moment (*20*) for the same initial stress. However, correcting for the different moments slightly reduces but does not remove the difference between thrust and normal fault motion near the fault trace. Whereas the amplified motion of the hanging wall decreases with increasing dip angle, the amplified motion of the thrust fault versus the normal fault increases with dip angle. This effect is also suggested in Fig. 2, where the difference in rupture criterion between the two faults increases between dips of 30° and 60° before returning to zero at 90°.

The results of our simulations may explain some observations in the vicinity of nonvertical dip-slip faults, such as increased ground motion in the hanging wall (*3–5*) and the observation that thrust faults produce greater ground motion than normal faults (*8*). Furthermore, the increased motion in the hanging wall near the free surface (relative to the motion at depth) will cause greater strain in the hanging wall, which could explain the often-observed cloud of aftershocks in the hanging walls above dip-slip faults (*21*).

There are some caveats to our simulations. First, it is possible that normal faults have zero or tensile normal stresses near the free surface, at which point the normal stress drops out of the friction law (*22*). However, our simulations with stress drop tapering to zero in the upper few hundred meters produced the same results. Furthermore, due to the effects of pore pressure and rock weakness, it is possible that faults are too weak in the upper 1 or 2 km to hold much fracture energy (*23*). Thus, the dynamic effects in real earthquakes with real surface geology may not be as pronounced as in this study, which is an end-member with the stress drop extending all the way to the free surface.

REFERENCES AND NOTES

1. A recent example of an earthquake in a compressional regime is the 1994 Northridge earthquake, which was modeled by D. Wald *et al*. [*Bull. Seismol. Soc. Am*. **86**, S49 (1996)]. One earthquake in an extensional regime is the 1983 Borah Peak, Idaho, earthquake, which is described by W. D. Richins *et al*. [*ibid*. **77**, 694 (1987)].
2. A normal fault is one in which the hanging wall moves down and outward with respect to the foot wall. A thrust or reverse fault is one in which the hanging wall moves up and inward with respect to the foot wall. A thrust fault has a dip angle <45° with respect to the free surface, and a reverse fault has a dip angle >45°. For simplicity, however, we will refer to all thrust and reverse earthquakes as thrust. The hanging wall of a dipping fault is defined as the block on top of the fault, which includes the acute angle with the free surface (Fig. 1). The footwall is the block below the fault, which includes the obtuse angle with the free surface.
3. N. Abrahamson and P. Somerville, *Bull. Seismol. Soc. Am.* **86**, S93 (1996).
4. K. Steinbrugge *et al.*, in *San Fernando, California, Earthquake of 9 February 1971*, G. Oakeshott, Ed. [*Calif. Div. Mines Geol. Bull.* **196**, 323 (1975)].
5. R. Nason, in *San Fernando, California, Earthquake of February 9, 1971*, L. Murphy, Ed. (U.S. Department of Commerce–NOAA, Washington, DC, 1973), vol. 3, p. 123.
6. P. Jungels and G. Frazier, *J. Geophys. Res.* **78**, 5062 (1973); T. Heaton, *Phys. Earth Planet. Int.* **64**, 1 (1990).
7. J. Brune, *Proc. Indian Acad. Sci.* (*Earth Planet. Sci.*) **105**, L197 (1996).
8. A. McGarr, *J. Geophys. Res.* **89**, 6969 (1984); N.

Abrahamson and K. Shedlock, *Seismol. Rev. Lett.* **68**, 9 (1997).
9. R. Whirley *et al.*, *DYNA2D: A Nonlinear, Explicit, Two-Dimensional Finite Element Code for Solid Mechanics—User Manual* (UCRL-MA-110630, University of California, Lawrence Livermore National Laboratory, Livermore, CA, 1992).
10. D. Andrews, *J. Geophys. Res.* **81**, 3575 (1976); *ibid.*, p. 5679; R. Archuleta, thesis, University of California, San Diego (1976); _____ and P. Frazier, *Bull. Seismol. Soc. Am.* **68**, 541 (1978); S. Day, *ibid.* **72**, 705 (1982); *ibid.*, p. 1881; A. Ruina, *J. Geophys. Res.* **88**, 10359 (1983); T. Mikumo and T. Miyatake, *Geophys. J. Int.* **112**, 481 (1993); R. Madariaga and A. Cochard, *Proc. Natl. Acad. Sci. U.S.A.* **93**, 3819 (1996).
11. Stresses in this report are defined according to Fig. 1. σ_x and σ_y are the normal stresses in the *x* and *y* directions; σ_n is the normal stress across the fault; σ_{xy} and σ_{yx} are the shear stresses in the *x* and *y* directions; τ is the (frictional) shear stress along the fault. The yield stress level is equal to $\mu\sigma_n$ where μ is the static frictional coefficient. The sliding frictional stress level is equal to $\mu'\sigma_n$, where μ' is the sliding frictional coefficient.
12. The stress drop is a cosine function from with a drop time of 0.2 s. This form corresponds to a slip-weakening friction law, with an effective slip-weakening distance (*15*) of 1 to 20 cm, depending on the slip rate.
13. We derive a general solution for the change in rupture criterion in a manner analogous to that of S. Nielsen [*Geophys. Rev. Lett.* **25**, 125 (1998)].
14. The stress field in the vicinity of a slip-weakening crack has been explored [Y. Ida, *J. Geophys. Res.* **77**, 3796 (1972); D. Andrews, *ibid.* **81**, 5679 (1976)].
15. J. Rudniki and M. Wu, *ibid.* **100**, 22173 (1995).
16. Breakout phases (large radiation pulses emitted when the rupture front breaks through the free surface) are examined in R. Burridge and G. Halliday, *Geophys. J. R. Astron. Soc.* **25**, 261 (1971).
17. B. J. Shi *et al.*, in preparation.
18. P. Davis and L. Knopoff, *Geophys. J. Int.* **106**, 581 (1991).
19. This may be an indication that our friction law or healing criterion, or both, may not be valid right at the free surface.
20. The seismic moment [K. Aki, *Bull. Earthquake Res. Inst. Tokyo Univ.* **44**, 73 (1966)] is the standard measurement for the absolute size of an earthquake and is defined as $M_0 = \mu\bar{s}A$, where μ is the shear modulus, $\bar{s}$ is the average slip on the fault, and *A* is the area on the fault in which slip occurred.
21. Examples of aftershock locations are seen in the 1983 Coalinga, California, earthquake; the 1981 Corinth, Greece, earthquake; the 1980 El Asnam, Algeria, earthquake; the 1982 Miramichi, Canada, earthquake [D. Eberhart-Phillips and P. Reasenberg, in *The Coalinga, California, Earthquake of May 2, 1983*, M. Rymer and W. Ellsworth, Eds., *U.S. Geol. Surv. Prof. Pap.* **1487**, 171 (1990)]; and the 1994 Northridge earthquake [H. Thio and H. Kanamori, *Bull Seismol. Soc. Am.* **86**, S84 (1996)].
22. Y. Zeng, personal communication; R. Sibson, personal communication.
23. Fault friction and weakness are discussed in detail in C. Scholz, *The Mechanics of Earthquakes and Faulting* (Cambridge Univ. Press, Cambridge, 1989), pp. 44–91.
24. J. Byerlee, *Pure Appl. Geophys.* **116**, 615 (1978).
25. Computations for this study were carried out primarily on the SGI Origin 2000 at the Materials Research Laboratory, University of California, Santa Barbara (UCSB) (NSF grant CDA96-01954). This research was supported by UCSB, UCSB/Campus Laboratory Collaboration grant 08950868, and Lawrence Livermore National Laboratory–Institute of Geophysics and Planetary Physics grant 98-GS012. S.B.N. was supported by the Materials Research Science and Engineering Center Program of the NSF under award DMR96-32716. This work is Institute for Crustal Studies contribution 0286-69EQ. The authors gratefully acknowledge the extensive programming advice of E. Zywicz and the support and advice of W. Foxall and L. Hutchings.

17 November 1997; accepted 18 March 1998

Percolation of Core Melts at Lower Mantle Conditions

M. C. Shannon and C. B. Agee

Experiments at high pressure and temperature to determine the dihedral angle of core melts in lower mantle phases yielded a value of ~71° for perovskite-dominated matrices. This angle, although greater than the 60° required for completely efficient percolation, is considerably less than the angles observed in mineral matrices at upper mantle pressure-temperature conditions in experiments. In other words, molten iron alloy can flow much more easily in lower mantle mineralogies than in upper mantle mineralogies. Accordingly, although segregation of core material by melt percolation is probably not feasible in the upper mantle, core formation by percolation may be possible in the lower mantle.

Core formation is by far the largest mass transfer event in Earth history. For a homogeneous chondritic Earth this event involves the separation of iron metal from silicate material to form a metallic core with an overlying silicate mantle. Two possible separation mechanisms have emerged (*1*): melt segregation through a molten matrix, a process commonly referred to as rainfall, and melt segregation through a solid matrix, usually termed percolation. Rainfall requires that some or all of the silicate mantle was molten, allowing the molten iron droplets to "fall" to the center as a result of their greater density. Percolation involves molten iron moving through solid rock by flowing between grains along an interconnected grain-edge pore network. Several experimental studies showed that percolation in the upper mantle would not be possible (*2–4*). The fluid-solid interfacial energy of molten iron and iron-sulfur alloys in lower mantle aggregates is too high, relative to the grain boundary energies of a rock matrix of olivine (and its higher pressure polymorphs), pyroxene, and garnet, to permit the melts to form an interconnected network. Percolation is therefore inefficient, stranding some of the metallic alloy in the silicate matrix. Because rock samples from the upper mantle show no evidence of stranded core material, true percolation is ruled out. In the lower mantle, however, the mineralogy changes to a matrix dominated by (Mg, Fe)SiO_3 perovskite and magnesiowuestite (*5*). The physical properties of perovskite and magnesiowuestite differ from those of olivine and pyroxene because of the coordination change of silicon from tetrahedral (coordinated to four oxygen atoms) to octahedral (coordinated to six oxygen atoms). It is unknown how iron alloy interacts with these lower mantle phases, although an enhanced percolation ability is suspected (*1*, *6*). Here we examined the ability of iron alloy to form an interconnected grain-edge network with perovskite and magnesiowuestite.

Experiments were performed with multi-anvil device; the experimental setup was similar to that described in (*7*) except that a carbon capsule was used to separate the starting material from the heater and no thermocouple was present. Temperature was estimated on the basis of power consumption and a comparison of textures from similar experiments run with a thermocouple (*8*). We used two starting materials: Homestead meteorite (an L5 ordinary chondrite) and a mixture of enstatite and iron sulfide. Both starting materials were ground to an average grain size of 5 to 10 μm. The materials were pressurized to ~25 GPa and heated to a point just below the silicate solidus where the silicates and oxides are solid and the iron alloy is molten, about 2100°C. These conditions were maintained for 3 hours to achieve a close approximation to textural equilibrium. In the 25-GPa runs, the original phases of Homestead recrystallized to form perovskite $(Mg_{.76}Fe_{.24})SiO_3$, magnesiowuestite $(Mg_{.35}Fe_{.65})O$, garnet, calcium perovskite, and quenched iron-nickel-sulfur melt ($Fe_{81}Ni_7S_{12}$) (Fig. 1A). The original enstatite recrystallized to form perovskite $(Mg_{.95}Fe_{.05})SiO_3$ in contact with quenched iron-sulfide melt ($Fe_{89}Ni_1S_{10}$) (Fig. 1B).

To characterize percolation ability, we determined the dihedral angle that the quenched alloy (molten during run conditions) forms with the solid silicate phases from the polished sections. Because the dihedral angle is measured in the plane normal to the axis of the triple junction between two solid grains and a quenched melt pocket, measured angles in a single section will produce a distribution of apparent angles (*9*). We approximate the true angle with the median of the distribution of apparent angles (*10*). A dihedral angle of 60° or less indicates that efficient percolation is

Department of Earth and Planetary Sciences, Harvard University, Cambridge, MA 02138, USA.